Sea-ice production in Antarctic coastal polynyas estimated from AMSR2 data and its validation using AMSR-E and SSM/I-SSMIS data

Sohey Nihashi, Kay I. Ohshima, and Takeshi Tamura

***Abstract*—Antarctic coastal polynyas are very high sea-ice production areas. The resultant large amount of brine rejection leads to the formation of dense water. The dense water forms Antarctic Bottom Water, which is the densest water in the global overturning circulation and a key player in climate change as a significant sink for heat and carbon dioxide. In this study, an algorithm was developed that uses AMSR2 data (2012–present) to detect polynya area and estimate thin ice thickness by a method similar to that used to develop the algorithm for AMSR-E data. Landfast sea-ice areas were also detected using AMSR2 data. Ice production in the polynyas was estimated by a heat flux calculation using AMSR2 sea-ice data. In four major polynyas, AMSR2 ice production was compared with AMSR-E (2003–2011) ice production through comparison of them with SSM/I-SSMIS ice production. The comparison confirmed that the ice production from AMSR-E/2 data, which have higher spatial resolution than SSM/I-SSMIS data, can be used to analyze time series covering more than 10 years. For example, maps of annual ice production based on AMSR-E/2 data revealed detailed changes of the Mertz Polynya, where the ice production decreased significantly after the Mertz Glacier Tongue calving in 2010. Continuous monitoring of the coastal polynyas by the AMSR series sensors is essential for climate-change-related analyses in the Antarctic Ocean.**

***Index Terms*—Advanced Microwave Scanning Radiometer 2 (AMSR2), Antarctic coastal polynyas, sea-ice production**

I. Introduction

Antarctic coastal polynyas are new/thin sea-ice areas formed by divergent ice motion driven by winds and ocean currents [1]. Since thin sea ice is a poor thermal barrier, it permits heat loss to the atmosphere one or two orders of magnitude larger than a thick ice cover does [2]; therefore, Antarctic coastal polynyas are areas of very high sea-ice production [3]–[5]. In the Antarctic Ocean, about 10% of sea ice is produced in the major coastal polynyas, although the total area of the polynyas is only about 1% of the maximum sea-ice area [5]. The resultant large amount of brine rejection leads to the formation of dense water [6], which is a major source of Antarctic Bottom Water (AABW) [7]–[11]. The sinking of the dense water plays a significant role in the global climate system by driving thermohaline (overturning) circulation [12] and biogeochemical cycles such as the exchange of carbon dioxide between the atmosphere and deep ocean [1], [13], [14]. Polynyas can also be biological "hot spots" during the spring and summer seasons [15].

Satellite remote sensing using passive microwave sensors can contribute greatly to hemispheric monitoring of coastal polynyas because microwave sensors can observe Earth's surface regardless of darkness or cloud cover. On the basis of comparisons between brightness temperatures (TBs) obtained from a passive microwave radiometer onboard a ship and sea-ice data from in situ measurements in the Canadian Arctic, it has been shown that the polarization ratio (PR) of TBs is negatively correlated with thin ice thickness of less than about 20 cm [16]. PR is defined as

$$PR = (TB_V - TB_H)/(TB_V + TB_H) \quad (1)$$

where TB_V and TB_H are the vertically and horizontally polarized TBs, respectively. Algorithms have been developed based on this relationship to detect Antarctic coastal polynyas and to estimate the thin ice thickness on a daily time scale from passive microwave satellite data, namely, TB data from the Special Sensor Microwave Imager (SSM/I) and the Special Sensor Microwave Imager/Sounder (SSMIS) on Defense Meteorological Satellite Program (DMSP) satellites [17], [18] and the Advanced Microwave Scanning Radiometer for EOS (AMSR-E) on the National Aeronautics and Space Administration's (NASA) Aqua satellite [19]. In these studies, thin ice thickness for the comparisons was based on heat flux calculations using ice surface temperatures from clear-sky satellite thermal infrared images. Circumpolar maps of ice production in Antarctic coastal polynyas were presented using thin ice thickness derived from the passive microwave satellite data with heat flux calculation [5], [19].

The width of the Antarctic coastal polynyas from the

Manuscript received December 19, 2016. This work was supported by a research fund for Global Change Observation Mission–Water 1 (GCOM-W1) of the Japan Aerospace eXploration Agency (JAXA). The AMSR2 data were provided by the JAXA. Comments from the reviewers were very helpful.

S. Nihashi is with the Department of Engineering for Innovation, National Institute of Technology, Tomakomai College, 443 Nishikioka, Tomakomai 059-1275, Japan (e-mail: sohey@tomakomai-ct.ac.jp).

K. I. Ohshima is with the Institute of Low Temperature Science, Hokkaido University, Kita-19, Nishi-8, Kita-ku, Sapporo 060-0819 (ohshima@lowtem.hokudai.ac.jp).

Takeshi Tamura is with the National Institute of Polar Research, Tachikawa, Tokyo 190-8518, Japan (tamura.takeshi@nipr.ac.jp), SOKENDAI (The Graduate University for Advanced Studies), Tachikawa, Tokyo 190-8518, Japan, and also with Antarctic Climate & Ecosystems Cooperative Research Centre, University of Tasmania, Hobart, Tasmania 7001, Australia.

coastline is about 100 km at most. Since the spatial (grid) resolution of AMSR-E data (about 6.25 km) is four times higher than that of SSM/I-SSMIS data (about 12.5 km) in pixel density, AMSR-E data can provide the detailed spatial distribution of thin ice thickness in a coastal polynya. A radar backscatter image of Cape Darnley Polynya (CDP) and Mackenzie Bay Polynya (MBP) in East Antarctica, acquired by the Advanced Synthetic Aperture Radar (ASAR: C-band SAR; the wavelength is 5.6 cm) on the European Space Agency's (ESA) Environmental Satellite (Envisat), and maps of thin ice thickness in the same area based on SSM/I and AMSR-E data are shown in Fig. 1. In this study, coastline, ice shelf, and glacier tongue locations were obtained from the National Snow and Ice Data Center (NSIDC) high-resolution Mosaic of Antarctica 2008–2009 (MOA2009) dataset, which has a spatial resolution of about 125 m [20]. In the ASAR image, the coastal polynyas appear as areas of white streaks with relatively high backscatter (>−10 dB). Both SSM/I and AMSR-E could detect CDP, although AMSR-E was better able to detect the polynya area, but only AMSR-E detected MBP, which is a narrow coastal polynya along the Amery Ice Shelf. In the Antarctic Ocean, landfast sea ice (fast ice) develops in many coastal areas. Fast ice is stationary sea ice attached to coastal features such as the shoreline and grounded icebergs [21]–[23]. A remarkable feature of the Antarctic Ocean is fast ice protruding into the ocean. Such fast ice is formed by grounded icebergs that act as anchor points [23]. Antarctic coastal polynyas tend to form adjacent to fast ice [19], and CDP also has formed on the western side of an area of fast ice. In the ASAR image (Fig. 1a), the low-backscatter (<−15 dB) area east of CDP is fast ice that is anchored by small grounded icebergs, which appear as small high-backscatter (>–5 dB) patches. Another fast ice area is developed to the west of CDP. Only AMSR-E detected these fast ice areas. These differences between SSM/I and AMSR-E are due to their different spatial resolutions. The details of the fast ice detection are described later. Although the AMSR-E mission ended in October 2011, its successor, the Advanced Microwave Scanning Radiometer 2 (AMSR2), on the Japan Aerospace Exploration Agency's (JAXA) Global Change Observation Mission 1st - Water (GCOM-W1; Shizuku) satellite was launched in May 2012. By combining AMSR2 data with AMSR-E data, a coastal polynya dataset with higher spatial resolution can be produced that covers >10 years. Such data are vital for understanding processes of the Antarctic coastal polynyas. In particular, the most useful information for understanding interactions between the climate system and Antarctic coastal polynyas is ice production, which leads to dense water and AABW formation. The primary purpose of this study is to generate an AMSR2 ice production dataset that in combination with AMSR-E ice production data would be suitable for times series studies. Therefore, we developed a thin ice thickness algorithm for AMSR2 by a method similar to that used to develop the AMSR-E algorithm [19], and we used it to estimate ice production in Antarctic coastal polynyas during 2012–2015. The AMSR2 ice production cannot be directly compared with the AMSR-E ice production because the observation periods do not overlap, whereas ice production data from SSM/I-SSMIS cover the entire AMSR-E/2 periods although they have a relatively coarse spatial resolution. Therefore, we assess the compatibility of ice production data between AMSR2 and AMSR-E by comparing each dataset with SSM/I-SSMIS ice production data. Then, by combining ice production data from AMSR2, AMSR-E, and SSM/I-SSMIS, we produce an ice production dataset covering >20 years, from the early 1990s to 2015.

II. Method And Data

A. Estimation of thin ice thickness

The method used to develop the thin ice thickness algorithm is explained briefly here. In the algorithm, ice thickness of ≤20 cm is estimated from PRs of AMSR2 TBs at 89 and 36.5 GHz. We used GCOM-W1/AMSR2 Level 1B (L1B) global swath TBs provided by JAXA's website (http://suzaku.eorc.jaxa.jp/GCOM_W/data/data_w_use.html). The footprint sizes are 5 km × 3 km and 12 km × 7 km at 89 and 36.5 GHz, respectively. These footprint sizes are about 85% of the size of the corresponding AMSR-E footprints owing to improvements of AMSR2. TBs at 89 GHz can minimize the contamination effects of land, ice shelf, and fast ice in areas close to the coast, where thinner ice is dominant, because of their relatively higher spatial resolution. On the other hand, the 89 GHz data possibly misclassify fast ice as thin ice, especially for the thickness range of >10 cm [24] (see also Section II-B). In this study, we used ice thicknesses of ≤ 10 cm estimated from TBs at 89 GHz along with ice thicknesses of 10–20 cm estimated from TBs at 36.5 GHz, which have a relatively deeper penetration depth.

To develop the AMSR2 thin ice thickness algorithm, AMSR2 PRs were compared with ice thickness based on heat flux calculations using ice surface temperatures from satellite thermal infrared images [25]. Ice thickness was estimated from the conductive heat flux in ice by assuming that it balances with the heat flux between ice and atmosphere. The snow cover on ice was neglected because new ice generally does not have a significant amount of snow cover. We used channel 31 and 32 thermal infrared images from the NASA Moderate Resolution Imaging Spectroradiometer (MODIS), specifically, MODIS Level 1B swath data with a spatial resolution of 1km provided by NASA's Level 1 and Atmosphere Archive and Distribution System website (LAADS web; http://ladsweb.nascom.nasa.gov/). We chose MODIS images that are free from cloud cover and ice fog during polar night, when shortwave radiation is negligible. Thus, the heat flux between ice and atmosphere is the sum of net longwave radiation and turbulent heat fluxes. We calculated ice surface temperatures with the empirical equation of [26] but modified it for use with MODIS data [27]–[29]. MODIS ice surface temperatures have been used previously to investigate long-term coastal polynya dynamics in the Weddell Sea [30]. Ice bottom temperature was set to the freezing point of –1.86°C. The heat flux between ice and atmosphere was calculated with equations suitable for the Antarctic sea-ice zone, following [31]. We used an empirical equation from [32] to calculate longwave

radiation. To calculate turbulent heat fluxes, we used bulk equations [33] with bulk transfer coefficients proposed by [34], which incorporate the stability effect of the atmospheric surface layer. As atmospheric input data, we used near-surface atmospheric data from the 6-hourly European Centre for Medium-Range Weather Forecasts (ECMWF) Interim Re-Analysis (ERA-Interim) dataset extracted at a resolution of 0.5° of latitude and longitude. Data of air temperature at 2 m, dewpoint temperature at 2 m, wind at 10 m, and surface sea level pressure (SLP) were used. The ERA-Interim data were interpolated onto the MODIS data points by using a Gaussian weighting function.

For the comparison with AMSR2 data, MODIS ice thickness with a spatial resolution of 1 km was remapped onto the data points of AMSR2 L1B data. There are dozens of MODIS pixels within each AMSR2 footprint. We used the thermal ice thickness for which the total heat flux calculated using MODIS data would be realized by assuming a uniform ice thickness in the AMSR2 footprint [17], [35]. The thermal ice thickness does not exactly coincide with the arithmetic average of the thicknesses calculated at MODIS pixels within the AMSR2 footprint. This thermal ice thickness (h_i) is suitable for heat loss calculations for the estimation of ice production.

Thin ice thickness calculated using AMSR2 L1B swath data at 89 and 36.5 GHz (h_{89} and h_{36}) was mapped onto the NSIDC polar stereographic grid at a spatial resolution of about 6.25 km and about 12.5 km, respectively. Afterward, the daily mean thickness was calculated by a simple sum-and-average mapping (drop-in-the-bucket) method. These grids are the same as those of the ice thickness from AMSR-E [19] and used for the comparison. Since one 12.5 km NSIDC grid cell corresponds to four 6.25-km NSIDC grid cells, $h_{89} \leq 10$ cm and h_{36} of 10–20 cm mapped at the two spatial resolutions can be merged directly. TBs at 89 GHz tend to be influenced by cloud cover, ice fog, and water vapor to a greater extent than TBs at 36.5 GHz. This leads to smaller values of PR at 89 GHz, and h_{89} is overestimated [17]. Since the atmospheric influence is less at 36.5 GHz, h_{89} is replaced with h_{36} of the corresponding pixel if $h_{89} \geq h_{36}$. The AMSR2 thin ice thickness algorithm can be used only to detect the thin ice area and to estimate its thickness; areas of open water and first-year ice must be detected by a different method. For that purpose, we used daily mean ice concentration in the AMSR2 level 2 swath product, estimated by using the Bootstrap algorithm [36]. We remapped the ice concentration onto the 12.5 km NSIDC grid. We defined an area with an ice concentration of <30% as open water. Then, among the remaining pixels, we labeled those with an estimated thickness of >20 cm in the thin ice algorithm as first-year ice.

B. Detection of landfast sea ice

The AMSR2 thin ice thickness algorithm can misclassify fast ice as thin ice because the PR values at 89 GHz of thin ice and fast ice can be similar within a certain thickness range [17], [37], especially for h_{89} >10 cm [24]. Thus, for accurate polynya detection, the independent detection of fast ice is essential. In this study, we adopted a method for fast ice detection that uses AMSR-E data (see [19] for details). Briefly, the detection of fast ice is based on its microwave characteristics: TBs of fast ice tend to be lower than those of thin ice and similar to those of the ice sheet. Thus, the detection method is not sensor dependent. Fast ice data for a given month were determined by using the daily TBs of three consecutive months, including the previous and the following month, based on the fact that fast ice is temporally more stable than thin ice. The monthly fast ice dataset also includes the variable ice-shelf edge, glacier tongues, and grounded iceberg tongues, all of which have microwave characteristics similar to those of an ice sheet.

C. Estimation of sea-ice production

In this study, a coastal polynya was defined as an area of sea-ice pixels (ice conc. ≥ 30%) with thickness ≤ 20 cm, and sea-ice production was estimated within such areas. The ice production was estimated on a daily basis from heat flux calculation using the daily mean AMSR2 thin ice thickness by a method similar to that used by the previous studies [5], [18], [19]. The sea-ice production rate V_i is estimated by assuming that heat from the ocean below is negligible and that all of the heat loss to the atmosphere contributes to the freezing of seawater, given by

$$V_i = \frac{Q}{\rho_i L_f}, \tag{2}$$

where Q (W m^{-2}) is heat loss to the atmosphere in a grid cell, ρ_i (=920 kg m^{-3}) is the density of sea ice, and L_f (=0.334 MJ kg^{-1}) is the latent heat of fusion for sea ice. This L_f value is based on [38] and has been used by many studies (e.g., [39], [40]). We obtained Q by assuming that the sum of radiative and turbulent fluxes at the ice surface is balanced by the conductive heat flux within the ice, the thickness of which is derived from the AMSR2 data. This heat flux calculation procedure is similar to that used to estimate thermal ice thickness from nighttime MODIS data, except for the inclusion of shortwave radiation in this procedure. Specifically, the clear-sky incoming shortwave radiation is calculated based on [41], with modification for the cloud cover [42]. We used the total cloud cover defined in the ERA-Interim dataset. Atmospheric input data from the daily ERA-Interim dataset were interpolated onto the NSIDC polar stereographic grid by using a Gaussian weighting function.

D. Comparisons among AMSR2, AMSR-E, and SSM/I-SSMIS data

We compared ice production from AMSR2, AMSR-E [19], and SSM/I-SSMIS [18] data in the four largest ice production polynya areas in the Antarctic Ocean: the Ross Ice Shelf Polynya (RISP), CDP, Mertz Polynya (MP), and Amundsen Polynya (AP). The polynya areas are indicated in Fig. 4 (the details of this figure are described later). Ice production in these four polynyas accounts for about 60% of total ice production in the 13 major Antarctic coastal polynyas [19]. Atmospheric input data for heat flux calculation of ice production from AMSR-E and SSM/I-SSMIS data is the same as in the case of

AMSR2 ice production (i.e., ERA-Interim data).

A small/narrow coastal polynya cannot be detected by SSM/I-SSMIS because of the relatively coarser spatial resolution (e.g., Fig. 1). This possibly leads to underestimation of ice production. Fast ice detection, which is also affected by the spatial resolution of the satellite sensor (e.g., Fig. 1), can also affect ice production estimates because Antarctic coastal polynyas tend to form adjacent to fast ice. For example, if an area of fast ice is not detected because of the relatively coarse spatial resolution of the sensor, ice production may be overestimated. The ice production estimate can also be affected by ambiguity in the thin ice thickness algorithms (PR–h_i relationships). We expect that the RISP to be suitable for ice production comparisons among AMSR2, AMSR-E, and SSM/I-SSMIS, because the polynya area is the largest and extensive fast ice does not develop. In contrast, detection of fast ice which forms near the CDP, MP, and AP would affect the ice production estimate. However, the effect is expected to be small because the size of these polynyas is relatively large. Cumulative monthly ice production calculated from AMSR2, AMSR-E, and SSM/I-SSMIS data are compared during the freezing period of March–October. To compare the AMSR2 and AMSR-E results, we first calculated a regression line of monthly ice production between SSM/I-SSMIS and AMSR-E. Then the consistency of the AMSR2 ice production result with the AMSR-E result was evaluated by comparing the AMSR2 result with this regression line.

III. Results

A. A thin ice thickness algorithm

A scatterplot of the AMSR2 PRs at 89 GHz (PR_{89}) versus MODIS h_i is shown in Fig. 2a. We used 186 clear-sky MODIS images of the RISP (96 scenes), Ronne Ice Shelf polynya (RONP) in the Weddell Sea (18 scenes), and CDP (72 scenes) acquired during April–September from 2013 to 2015. These three polynyas are major source areas of AABW [11], [43], [44]. For the plot, we used the AMSR2 L1B swath data acquired at times close to the MODIS image acquisition times. For each of three polynyas, PR_{89} and h_i were negatively correlated and the relationship was roughly similar among them. A scatterplot of the PRs at 36.5GHz (PR_{36}) versus h_i (Fig. 2b) shows a similar relationship. Moreover, from SSM/I and AMSR-E data, similar negatively correlated relationships have been found in the Arctic Ocean, the Sea of Okhotsk, along the Labrador coast, and the Antarctic Ocean [17], [19], [24], [45]–[49].

Thin ice thickness from AMSR2 data was estimated from exponential curves that best fit into the scatterplots of the PR versus h_i (Fig. 2). For the fitting, the normal from each data to the curve was calculated using only data with $h_i < 30$ cm, and then a least squares fitting was applied to minimize the distance. The equations derived by fitting a curve to data for all three polynyas are

$$h_{89} = e^{\frac{1}{104PR_{89}-0.07}} - 1.07 \text{ and} \quad (3)$$

$$h_{36} = e^{\frac{1}{72PR_{36}}} - 1.08, \quad (4)$$

where h_{89} and h_{36} are ice thicknesses estimated from PR_{89} and PR_{36}, respectively. The curves described by (3) and (4) are shown in Fig. 2. We confirmed that h_{89} and h_{36} coincide with each other with a root-mean-square deviation (RMSD) of about 1–2 cm in the case of a clear sky (not shown).

We summarize the h_i versus h_{89} and h_{36} statistics for each polynya and for all three polynyas together in Table I. For $PR_{89} \geq 0.062$ (i.e., $h_{89} \leq 10$ cm) the RMSD for all polynyas is 5.6 cm, and the biases (h_i minus h_{89}) range from 0.8 to 3.8 cm among the three polynyas. For PR_{36} of 0.057–0.083 (h_{36} of 10–20 cm), the RMSD for all polynyas is 5.8 cm, and the biases (h_i minus h_{36}) range from –3.6 to 1.6 cm among the three polynyas. As in the case of the AMSR-E thin ice thickness algorithm [19], the values of these deviations and biases are generally within the accuracy of h_i (about ±5 cm) determined by comparisons with in situ observations [35], [46], [50]. Therefore, we used (3) and (4) as a unified algorithm for the estimation of thin ice thickness from AMSR2 data over the entire Antarctic Ocean.

The relationships between AMSR-E PRs and MODIS h_i, taken from [19] (Fig. 2, black curves), are similar to those between AMSR2 PRs values and MODIS h_i (yellow curves) at both 89 GHz and 36.5 GHz, although the AMSR2 relationships are slightly shifted to thinner ice thickness by 1–2 cm. Although the AMSR-E mission ended in October 2011 because of a problem with the rotation of its antenna, AMSR-E Slow Rotation Data (2 rotations per minute) were acquired from 4 December 2012 to 4 December 2015. A comparisons of TBs obtained by AMSR2 and AMSR-E (with slow rotation) were made by "Intercomparison results between AMSR2 and TMI/AMSR-E/GMI (AMSR2 ver. 2.0) EORC JAXA" (downloaded at http://suzaku.eorc.jaxa.jp/GCOM_W/materials/product/150326_AMSR2_XcalResults.pdf). The comparison showed that the AMSR2 TBs over the ocean tended to be a few degrees higher than the AMSR-E TBs indicating that PR values from the AMSR2 data would be smaller than those from the AMSR-E data (1). The result of this comparison explains in part the difference between the fitted curves, although the comparison did not include areas of the ocean covered by sea ice.

We compared maps of thin ice thickness and fast ice from AMSR2 data for areas around the RISP, RONP, CDP, and MBP with 23 SAR images acquired by C-band SAR (C-SAR) on the ESA's Sentinel-1 satellite, which have a spatial resolution of about 90 m (e.g., Fig. 3). In most cases, including the examples shown in Fig. 3, thin ice and fast ice areas detected by using the AMSR2 data correspond well to their areas in the C-SAR images. This result supports the reliability of the AMSR2 algorithms.

B. Comparison of AMSR2 ice production with SSM/I-SSMIS and AMSR-E ice production

A circumpolar map of annual sea-ice production (cumulative ice production during March–October) and fast ice, averaged over 2013–2015 (Fig. 4), confirms that most polynyas have

formed on the western side of fast ice or a glacier tongue, indicating their close relationship. The spatial distributions of ice production and fast ice were generally similar to those determined from AMSR-E data for 2003–2010 [19, Fig. 9], except in the MP area. Annual ice production in the four major polynyas (RISP, CDP, MP, and AP) averaged over the AMSR2 (2013–2015) and AMSR-E (2003–2010) periods (Table II) revealed a significant (>50%) decrease in ice production in the MP area. The details of this drastic ice production decrease are described later.

Annual ice production calculated using SSM/I-SSMIS data is overestimated by about 5–30% compared with AMSR-E/2 ice productions, except in the MP area during 2013–2015 (Table II). This overestimation of ice production is attributed to the thin ice thickness algorithm (PR–h_i relationship). The PR–h_i relationship in SSM/I-SSMIS data is represented by a linear line (Fig. 2, dashed lines). On the other hand, the PR–h_i relationships in the AMSR-E/2 data are represented by exponential curves. The ice thickness is set at 1 cm, when the thickness is estimated from the fitted curve is <1 cm. The PR–h_i relationships (Fig. 2) show that thin ice thickness is unrealistically underestimated by SSM/I-SSMIS data when the PR value is high (i.e., ice thickness is thin; Fig. 1), which causes the overestimation of ice production.

Next, we compared monthly ice production in the RISP, CDP, MP, and AP between SSM/I-SSMIS (V_S) and AMSR-E (V_{AE}) and AMSR2 (V_{A2}) (Fig. 5). As expected, V_S was strongly correlated with both V_{AE} and V_{A2} with a significance level of >99.9%. Therefore, AMSR2 ice production can be compared with AMSR-E ice production by comparing each with SSM/I-SSMIS ice production. The regression lines obtained for all four polynyas from the V_S–V_{AE} relationship by least-squares fitting were similar (Fig. 5). For all polynyas, >95% of the AMSR2 data points fell within two standard deviations of the V_S–V_{AE} regression line; this result indicates that the regression lines obtained for the V_S–V_{AE} relationships can explain the V_S–V_{A2} relationships well. Further, both the biases and RMSDs of the data points of the V_S–V_{A2} relationships relative to the regression lines are small (Table III). These results suggest that combined AMSR-E/2 ice production data can be used for time series studies covering >10 years, from 2003. Outliers from the regression lines (e.g., in the RISP and CDP areas; Figs. 5a, b), is data collected during the ice-advance season (March–June) and are caused by discrepant detection (estimation) of thin ice and fast ice areas between SSM/I-SSMIS and AMSR-E/2. However, only 1% of the total data is affected, so the effect on the annual ice production estimates is quite small.

We examined whether the differences between the PR–h_i curves for AMSR2 and AMSR-E data (Fig. 2, yellow and black curves, respectively) were significant by estimating AMSR2 ice production from thin ice thickness estimated using the curves for the AMSR-E data [19]. Comparison of the results with the regression lines obtained for the V_S–V_{AE} relationships in the four polynyas (Fig. 5) showed that AMSR2 monthly ice production was underestimated by 10–25%. This underestimation is significant when it is compared with AMSR2 ice production in which thin ice thickness was estimated using the curves for the AMSR2 data (Table III). This result confirms that the AMSR2 thin ice thickness should be estimated using the new curves (Fig. 2 and Eqs. 3 and 4).

Annual ice production during >20 years (1992–present) can be obtained from the SSM/I-SSMIS data. Monthly ice production from SSM/I-SSMIS is highly correlated with AMSR-E/2 ice production, although the SSM/I-SSMIS ice productions is overestimated (Fig. 5). We consider that the higher spatial (grid) resolution of the AMSR-E/2 data provide more reliable thin ice thickness estimation and fast ice detection. The weakness of the AMSR-E/2 data due to the shorter measurement period and that of the SSM/I-SSMIS data due to their coarser spatial resolution can be somewhat mitigated considering AMSR-E (2003–2010) and AMSR2 (2013–2015) ice production together with SSM/I-SSMIS (1992–2002, 2011–2012) ice production. To combine the three datasets, we adjusted SSM/I-SSMIS ice production based on its relationship with AMSR-E/2 ice production (Table III and Fig. 5). The resulting time series of annual ice production in the RISP, CDP, MP, and AP are shown in Fig. 6. In the RISP, large ice production reduction events occurred in 2000 and 2002 (Fig. 6a) because giant icebergs (B-15 and C-19) that calved from the Ross Ice Shelf occupied the polynya during the freezing season [5], [51].

The MP time series (Fig. 6c) reveals that a drastic change occurred in 2010, after the calving of the Mertz Glacier Tongue (MGT). The MGT calving event led to a substantial decrease in the size of the MP and ice production [52]. The amount of ice production decreased by as much as 40%, and the MP dropped from the third to the fifth-largest Antarctic polynya in terms of ice production [19]. According to [18], the time series of SSM/I-SSMIS ice production until 2013 shows a continuous decrease in ice production after the MGT calving, but the analysis area used by [18] includes areas east of the MP not included in our study. Hydrographic observations made before and after the calving have clarified a significant reduction in dense water export and AABW formation [53], [54]. A numerical modeling simulation also predicted this reduction [55]. Further, significant changes in biogeochemical conditions also occurred after the MGT calving [56]. Analysis of a sediment core drilled in this region covering 250 years suggested that large and abrupt changes in local sea-ice and bottom-water conditions occur with a 70-year periodicity in association with MGT calving and regrowth dynamics [57]. These demonstrate a strong linkage between the glacier tongue and sea-ice/AABW production. Annual maps of AMSR-E/2 ice production (Fig. 7) can reveal the details of the MP change. Before 2010, westward advection of sea ice was blocked by the MGT and an offshore extension consisting of fast ice and grounded icebergs (sometimes referred to as the “dagger”); as a result, the MP was the third-largest polynya in terms of ice production. This fast ice dagger forms each winter and extends northward along the eastern edge of an area of shallow water called the Mertz Bank [22], [52], [58], [59]. However, since the 2010 calving event, the area of the MP has been divided into two areas of high ice production: one is located along the coast, and the other is west of the dagger (fast ice) in the offshore area.

Moreover, the area of high ice production west of the MGT disappeared. These mapping results clearly demonstrate the blocking effect of sea ice by the MGT. Further, the maps also reveal the linkage between a coastal polynya and fast ice. Since the MGT calving, an area of fast ice has developed in the western MP area (Fig. 7) that suppresses coastal polynya development and ice production there (Fig. 6c).

IV. Conclusions

A new algorithm for thin ice thickness in the Antarctic Ocean for AMSR2 data (2012–present) was developed (Fig. 2; Eqs 3 and 4) by a method similar to that used for the AMSR-E algorithm development [19]. From heat flux calculations using AMSR2 thin ice thickness, daily ice production in Antarctic coastal polynyas was estimated with a higher spatial resolution of about 6 km (Fig. 4). Since the periods covered by AMSR2 and AMSR-E data do not overlap, we compared AMSR2 ice production with AMSR-E ice production through a comparison with SSM/I-SSMIS ice production (Table III, Fig. 5). The results confirmed that the high-spatial-resolution ice production dataset from AMSR-E/2 can be used for time series studies covering >10 years. The disadvantage of the AMSR-E/2 ice production data is the relatively shorter period of the record compared with SSM/I-SSMIS ice production data, which has accumulated for >20 years. However, this weakness of the AMSR-E/2 dataset can be somewhat mitigated by combining it with the SSM/I-SSMIS ice production dataset (Fig. 6). For this, SSM/I-SSMIS ice production was adjusted based on the comparison results (Table III, Fig. 5).

The fact that most Antarctic coastal polynyas form on the western side of fast ice or glacier tongues [19] (Fig. 4) confirms that fast ice and glacier tongues protruding into the ocean are a key factor leading to the formation of many Antarctic coastal polynyas. Fast ice and glacier tongues are particularly vulnerable to oceanic and atmospheric conditions, and their extent can change drastically and suddenly. In turn, changes in the extent of fast ice or in the length of a glacier tongue can cause dramatic changes in sea-ice production in adjacent polynyas and, possibly, AABW formation, as was reported after the MGT calving event [52]–[57]. These changes potentially contribute to further climate change. AMSR-E/2 ice production data revealed the details of MP changes after the MGT calving (Fig. 7). Moreover, the MP time series revealed another role of fast ice in coastal polynya formation: fast ice development in an area that had been occupied by a polynya suppresses the ice production (Figs. 6c and 7). Since the spatial scale of coastal polynyas and fast ice (glacier tongues) is relatively small (typically <100 km), continuous monitoring of coastal polynyas and fast ice by AMSR series sensors, including the expected successor of AMSR2, is important for understanding the climate system.

References

[1] M. A. Morales Maqueda, A. J. Willmott, and N. R. T. Biggs, "Polynya dynamics: A review of observations and modeling," *Rev. Geophys., 42*, RG1004, doi:10.1029/2002RG000116, 2004.

[2] G. A, Maykut, "Energy exchange over young sea ice in the central Arctic," *J. Geophys. Res., 83*, 3646–3658, doi:10.1029/JC083iC07p03646, 1978.

[3] T. Markus, C. Kottmeier, and E. Fahrbach, "Ice formation in coastal polynyas in the Weddell Sea and their impact on oceanic salinity," *Antarctic Sea Ice: Physical Processes, Interactions, and Variability*, M. O. Jeffries, Ed., American Geophysical Union, Antarctic Research Series, 74, 273–292, 1998.

[4] I. A. Renfrew, J. C. King, and T.Markus, "Coastal polynyas in the southern Weddell Sea: Variability of the surface energy budget," *J. Geophys. Res., 107*, 3063, doi:10.1029/2000JC000720, 2002.

[5] T. Tamura, K. I. Ohshima, and S. Nihashi, "Mapping of sea ice production for Antarctic coastal polynyas," *Geophys. Res. Lett., 35*, L07606, doi:10.1029/2007GL032903, 2008.

[6] G. D. Williams, N. L. Bindoff, S. J. Marsland, and S. R. Rintoul, "Formation and export of dense shelf water from the Adélie Depression, East Antarctica," *J. Geophys. Res., 113*, C04039, doi:10.1029/2007JC004346, 2008.

[7] A. L. Gordon, B. A. Huber, H. H. Hellmer, and A. Field, "Deep and bottom water of the Weddell Sea's western rim," *Science, 262*, 95–97, doi:10.1126/science.262.5130.95, 1993.

[8] J. C. Comiso and A. L. Gordon, "Interannual variability in summer sea ice minimum, coastal polynyas and bottom water formation in the Weddell Sea," *Antarctic Sea Ice: Physical Processes, Interactions, and Variability*, M. O. Jeffries, Ed., American Geophysical Union, Antarctic Research Series, Vol. 74, 293–315, 1998.

[9] S. R. Rintoul, "On the origin and influence of Adélie Land Bottom Water," *Ocean, Ice, and Atmosphere: Interactions at the Antarctic Continental Margin*, S. S. Jacobs and R. F. Weiss, Eds., American Geophysical Union, Antarctic Research Series, Vol. 75, 151–171, 1998.

[10] G. D. Williams, S. Aoki, S. S. Jacobs, S. R. Rintoul, T. Tamura, and N. L. Bindoff, "Antarctic Bottom Water from the Adélie and George V Land coast, East Antarctica (140°–149°E)," *J. Geophys. Res., 115*, C04027, doi:10.1029/2009JC005812, 2010.

[11] K. I. Ohshima et al., "Antarctic Bottom Water production by intense sea-ice formation in the Cape Darnley polynya," *Nat. Geosci., 6*, 235–240, doi:10.1038/ngeo1738, 2013.

[12] P. D. Killworth, "Deep convection in the World Ocean," *Rev. Geophys., 21*, 1–26, doi:10.1029/RG021i001p00001, 1983.

[13] L. A. Miller and G. R. DiTullio, "Gas fluxes and dynamics in polynyas," *Polynyas: Windows to the World's Oceans,* W. O. Smith, Jr. and D. G. Barber, Eds., Elsevier, 163–191, 2007.

[14] M. Hoppema and L. G. Anderson, "Biogeochemistry of polynyas and their role in sequestration of anthropogenic constituents," *Polynyas: Windows to the World's Oceans*, W. O. Smith, Jr. and D. G. Barber, Eds., Elsevier, 193–221, 2007.

[15] K. R. Arrigo and G. L. van Dijken, "Phytoplankton dynamics within 37 Antarctic coastal polynya systems," *J. Geophys. Res., 108*, 3271, doi:10.1029/2002JC001739, 2003.

[16] B. J. Hwang, J. K. Ehn, D. G. Barber, R. Galley, and T. C. Grenfel, "Investigations of newly formed sea ice in the Cape Bathurst polynya: 2. Microwave emission," *J. Geophys. Res., 112*, C05003, doi:10.1029/2006JC003703, 2007.

[17] T. Tamura, K. I. Ohshima, T. Markus, D. J. Cavalieri, S. Nihashi, and N. Hirasawa, "Estimation of thin ice thickness and detection of fast ice from SSM/I data in the Antarctic Ocean," *J. Atmos. Oceanic Technol., 24*, 1757–1772, doi:10.1175/JTECH2113.1, 2007.

[18] T. Tamura, K. I. Ohshima, A. D. Fraser, and G. D. Williams, "Sea ice production variability in Antarctic coastal polynyas," *J. Geophys. Res., 121*, doi:10.1002/2015JC011537, 2016.

[19] S. Nihashi and K. I. Ohshima, "Circumpolar mapping of Antarctic coastal polynyas and landfast sea ice: relationship and variability," *J. Clim., 28*, 3650–3670, DOI: 10.1175/JCLI-D-14-00369.1, 2015.

[20] T. Haran, J. Bohlander, T. Scambos, T. Painter, and M. Fahnestock, "MODIS Mosaic of Antarctica 2008-2009 (MOA2009) image map," National Snow and Ice Data Center, Boulder, CO, http://dx.doi.org/10.7265/N5KP8037, 2014.

[21] WMO, WMO sea-ice nomenclature, terminology, codes and illustrated glossary. WMO/OMM/BMO Rep. 259, Tech. Paper 145, World Meteorological Organization, 147 pp, 1970.

[22] R. A. Massom, K. L. Hill, V. I. Lytle, A. P. Worby, M. J. Paget, and I. Allison, Effects of regional fast-ice and iceberg distributions on the behaviour of the Mertz Glacier polynya, East Antarctica, *Ann. Glaciol.*, *33*, 391–398, doi:10.3189/172756401781818518.2001.

[23] A. D. Fraser, R. A. Massom, K. J. Michael, B. K. Galton-Fenzi, and J. L. Lieser, East Antarctic landfast sea ice distribution and variability, 2000–08. *J. Climate*, *25*, 1137–1156, doi:10.1175/JCLI-D-10-05032.1, 2012.

[24] K. Iwamoto, K. I. Ohshima, and T. Tamura, "Improved mapping of sea ice production in the Arctic Ocean using AMSR-E thin ice thickness algorithm," *J. Geophys. Res.*, *119*, 3574–3594, doi:10.1002/2013JC009749, 2014.

[25] Y. Yu and D. A. Rothrock, "Thin ice thickness from satellite thermal imagery," *J. Geophys. Res.*, *101*, 25,753–25,766, doi:10.1029/96JC02242, 1996.

[26] J. Key, J. B. Collins, C. Fowler, and R. S. Stone, "Highlatitude surface temperature estimates from thermal satellite data," *Remote Sens. Environ.*, *61*, 302–309, doi:10.1016/S0034-4257(97)89497-7, 1997.

[27] D. K. Hall, J. R. Key, K. A. Casey, G. A. Riggs, and D. J. Cavalieri, "Sea ice surface temperature product from MODIS," *IEEE Trans. Geosci. Remote Sens.*, *42*, 1076–1087, doi:10.1109/TGRS.2004.825587, 2004.

[28] G. A. Riggs, D. K. Hall, and V. V. Salomonson, "MODIS sea ice products user guide to collection 5," NASA Goddard Space Flight Center, Greenbelt, MD, 49 pp. [Available online at http://modis-snow-ice.gsfc.nasa.gov/uploads/siug_c5.pdf.], 2006.

[29] T. A. Scambos, T. M. Haran, and R. Massom, "Validation of AVHRR and MODIS ice surface temperature products using in situ radiometer," *Ann. Glaciol.*, *44*, 345–351, doi:10.3189/172756406781811457, 2006.

[30] S. Paul, S. Willmes, and G. Heinemann, "Long-term coastal-polynya dynamics in the southern Weddell Sea from MODIS thermal-infrared imagery," *The Cryosphere*, *9*, 2027–2041, doi:10.5194/tc-9-2027-2015, 2015.

[31] S. Nihashi and K. I. Ohshima, "Relationship between ice decay and solar heating through open water in the Antarctic sea ice zone," *J. Geophys. Res.*, *106*, 16,767–16,782, doi:10.1029/2000JC000399, 2001.

[32] G. König-Langlo and E. Augstein, "Parameterization of the downward longwave radiation at the Earth's surface in polar regions," *Meteor. Z.*, *3*, 343–347, 1994.

[33] G. A. Maykut and D. K. Perovich, "The role of shortwave radiation in the summer decay of a sea ice cover," *J. Geophys. Res.*, *92*, 7032–7044, doi:10.1029/JC092iC07p07032, 1987.

[34] J. Kondo, "Air–sea bulk transfer coefficient in diabatic conditions," *Bound.-Layer Meteor.*, *9*, 91–112, doi:10.1007/BF00232256, 1975.

[35] R. Drucker, S. Martin, and R. Moritz, "Observations of ice thickness and frazil ice in the St. Lawrence Island polynya from satellite imagery, upward looking sonar, and salinity/temperature moorings," *J. Geophys. Res.*, *108*, 3149, doi:10.1029/2001JC001213, 2003.

[36] J. C. Comiso, "SSM/I Ice Concentrations Using the Bootstrap Algorithm", NASA RP 1380, 1995.

[37] S. Kern, "Wintertime Antarctic coastal polynya area: 1992–2008," *Geophys. Res. Lett.*, *36*, L14501, doi:10.1029/2009GL038062, 2009.

[38] S. Martin, "Frazil ice in rivers and oceans," *Annu. Rev. Fluid Mech.*, *13*, 379–397, doi:10.1146/annurev.fl.13.010181.002115, 1981.

[39] D. J. Cavalieri and S. Martin, "The contribution of Alaskan, Siberian, and Canadian coastal polynyas to the cold halocline layer of the Arctic Ocean," *J. Geophys. Res.*, *99*, 18,343–18,362, doi:10.1029/94JC01169, 1994.

[40] G. Fusco, D. Flocco, G. Budillon, G. Spezie, and E. Zambianchi, "Dynamics and variability of Terra Nova Bay Polynya," *PSZN Marine Ecology*, *23*, 201–209, doi:10.1111/j.1439-0485.2002.tb00019.x., 2002.

[41] J. W. Zillman, "A study of some aspects of the radiation and heat budgets of the Southern Hemisphere oceans," Department of the Interior, Bureau of Meteorology, Canberra, Meteorological Studies Series, Vol. 26, 562 pp, 1972.

[42] R. K. Reed, "On estimating insolation over the ocean," *J. Phys. Oceanogr.*, *7*, 482–485, doi:10.1175/1520-0485(1977)007,0482: OEIOTO.2.0.CO;2, 1977.

[43] S. S. Jacobs, A. F. Amos, and P. M. Bruchhausen, "Ross Sea oceanography and Antarctic Bottom Water formation," *Deep-Sea Res. Oceanogr. Abstr.*, *17*, 935–962, doi:10.1016/0011-7471(70)90046-X, 1970.

[44] T. D. Foster and E. C. Carmack, "Frontal zone mixing and Antarctic Bottom Water formation in the southern Weddell Sea," *Deep-Sea Res. Oceanogr. Abstr.*, *23*, 301–317, doi:10.1016/0011-7471(76)90872-X, 1976.

[45] S. Martin, R. Drucker, R. Kwok, and B. Holt, "Estimation of the thin ice thickness and heat flux for the Chukchi Sea Alaskan coast polynya from Special Sensor Microwave/Imager data, 1990–2001," *J. Geophys. Res.*, *109*, C10012, doi:10.1029/2004JC002428, 2004.

[46] S. Nihashi, K. I. Ohshima, T. Tamura, Y. Fukamachi, and S. Saitoh, "Thickness and production of sea ice in the Okhotsk Sea coastal polynyas from AMSR-E," *J. Geophys. Res.*, *114*, C10025, doi:10.1029/2008JC005222, 2009.

[47] T. Tamura and K. I. Ohshima, "Mapping of sea ice production in the Arctic coastal polynyas," *J. Geophys. Res.*, *116*, C07030, doi:10.1029/2010JC006586, 2011.

[48] K. Iwamoto, K. I. Ohshima, T. Tamura, and S. Nihashi, "Estimation of thin ice thickness from AMSR-E data in the Chukchi Sea," *Int. J. Remote Sens.*, *34*, 468–489, doi:10.1080/01431161.2012.712229, 2013.

[49] K. A. Scott, M. Buehner, and T. Carrieres, "An assessment of sea-ice thickness along the Labrador coast from AMSR-E and MODIS data for operational data assimilation," *IEEE Trans. Geosci. Remote Sens.*, *52*, 2726–2737, doi:10.1109/TGRS.2013.2265091, 2014.

[50] T. Tamura, K. I. Ohshima, H. Enomoto, K. Tateyama, A. Muto, S. Ushio, and R. A. Massom, "Estimation of thin sea-ice thickness from NOAA AVHRR data in a polynya off the Wilkes Land coast, East Antarctica," *Ann. Glaciol.*, *44*, 269–274, doi:10.3189/172756406781811745, 2006.

[51] S. Martin, R. S. Drucker, and R. Kwok, The areas and ice production of the western and central Ross Sea polynyas, 1991–2002, and their relation to the B-15 and C-19 iceberg events of 2000 and 2002, *J. Mar. Syst.*, *68*, 201–214, 2007.

[52] T. Tamura, G. D. Williams, A. D. Fraser, and K. I. Ohshima, "Potential regime shift in decreased sea ice production after the Mertz Glacier calving," *Nat. Commun.*, *3*, 826, doi:10.1038/ncomms1820, 2012.

[53] S. Aoki, Y. Kitade, K. Shimada, K. I. Ohshima, T. Tamura, C. C. Bajish, M. Moteki, and S. R. Rintoul, "Widespread freshening in the Seasonal Ice Zone near 140°E off the Adélie Land Coast, Antarctica, from 1994 to 2012," *J. Geophys. Res.*, *118*, 6046–6063, doi: 10.1002/2013JC009009, 2013.

[54] M. Lacarra, M. N. Houssais, C. Herbaut, E. Sultan, and M. Beauverger, "Dense shelf water production in the Adélie Depression, East Antarctica, 2004–2012: Impact of the Mertz Glacier calving," *J. Geophys. Res.*, *119*, 5203–5220, doi:10.1002/2013JC009124, 2014.

[55] K. Kusahara, K., H. Hasumi, and G. D. Williams, "Impact of Mertz Glacier Tongue calving on dense water formation and export," *Nat. Commun.*, *2*, 159, doi:10.1038/ncomms1156, 2011.

[56] E. Shadwick, S. R. Rintoul, B. Tilbrook, G. D. Williams, N. Young, A. D. Fraser, H. Marchant, J. Smith, and T. Tamura, "Glacier tongue calving reduced dense water formation and enhanced carbon uptake," *Geophys. Res. Lett.*, 40, 904–909, doi:10.1002/grl.50178, 2013.

[57] P. Campagne, X. Crosta, M. N. Houssais, D. Swingedouw, S. Schmidt, A. Martin, E. Devred, S. Capo, V. Marieu, I. Closset, G. Masse', "Glacial ice and atmospheric forcing on the Mertz Glacier Polynya over the past 250 years," *Nat. Commun.*, *6*, 6642, doi:10.1038/ncomms7642, 2015.

[58] R. A. Massom, "Recent iceberg calving events in the Ninnis Glacier region, East Antarctica," *Antarct. Sci.*, 15, 303–313, doi:10.1017/S0954102003001299, 2003.

[59] R. A. Massom, A. B. Giles, H. A. Fricker, R. C. Warner, B. Legrésy, G. Hyland, N. Young, and A. D. Fraser, "Examining the interaction between multi-year landfast sea ice and the Mertz Glacier Tongue, East Antarctica: Another factor in ice sheet stability?," *J. Geophys. Res.*, 115, C12027, doi:10.1029/2009JC006083, 2010.

TABLE I
STATISTICS OF THE RELATIONSHIP BETWEEN h_i FROM MODIS AND h_{89} AND h_{36} FROM AMSR2 (FIG. 2) FOR THREE POLYNYAS.

Polynya	RMSD (cm)	SD (cm)	Bias (cm)	Sample No.
		$h_{89} \le 10$ cm ($PR_{89} \ge 0.062$)		
RISP	6.1	4.7	3.8	18061
RONP	3.9	3.9	0.8	2172
CDP	5.1	4.7	2.0	9984
ALL	5.6	4.8	3.0	30217
		$10 < h_{36} \le 20$ cm ($0.057 < PR_{36} \le 0.083$)		
RISP	5.7	5.5	1.6	3418
RONP	5.8	4.6	–3.6	301
CDP	7.4	7.1	–1.9	270
ALL	5.8	5.7	1.0	3989

RMSD and SD are the root-mean-square deviation and the standard deviation, respectively. Bias is h_i minus h_{89} or h_{36}. RISP, RONP, CDP, and ALL indicate the Ross Ice Shelf Polynya, Ronne Ice Shelf Polynya, Cape Darnley Polynya, and all of the three polynya areas, respectively.

TABLE II
ANNUAL ICE PRODUCTION (CUMULATIVE ICE PRODUCTION DURING MARCH–OCTOBER) AVERAGED OVER THE AMSR-E (2003—2010) AND AMSR2 (2013—2015) PERIODS WITH ITS ANNUAL STANDARD DEVIATION.

	Annual ice production (10^9 m^3)			
	2003—2010		2013—2015	
Polynya	SSM/I-SSMIS	AMSR-E	SSM/I-SSMIS	AMSR2
RISP	316 ± 34	300 ± 20	340 ± 32	317 ± 18
CDP	153 ± 19	134 ± 12	155 ± 12	137 ± 13
MP	139 ± 25	132 ± 18	55 ± 4	61 ± 2
AP	110 ± 16	90 ± 13	117 ± 22	90 ± 17

RISP, CDP, MP, and AP indicate the Ross Ice Shelf Polynya, Cape Darnley Polynya, Mertz Polynya, and Amundsen Polynya, respectively. The analysis areas are indicated in Fig. 4.

TABLE III
STATISTICS OF THE RELATIONSHIP BETWEEN MONTHLY AMSR2 ICE PRODUCTION AND THE REGRESSION LINES RELATING SSM/I-SSMIS ICE PRODUCTION WITH AMSR-E ICE PRODUCTION IN FOUR POLYNYAS (FIG. 5).

Polynya	Bias (10^9 m^3)	RMDS (10^9 m^3)	Ratio of bias (%)	Ratio of RMDS (%)
RISP	0.7	3.4	2.4	8.0
CDP	0.1	1.5	0.2	9.1
MP	–1.2	1.4	–13.9	16.4
AP	–0.8	1.3	–8.5	16.4

Bias is the ice production from AMSR2 minus that from the regression line. RMSD is the root-mean-square deviation of the data points of AMSR2 relative to the regression line. The ratios of bias and RMSD are the bias and RMSD normalized by dividing by the ice production from the regression line. RISP, CDP, MP, and AP indicates the Ross Ice Shelf Polynya, Cape Darnley Polynya, Mertz Polynya, and Amundsen Polynya, respectively. The analysis areas are indicated in Fig. 4.

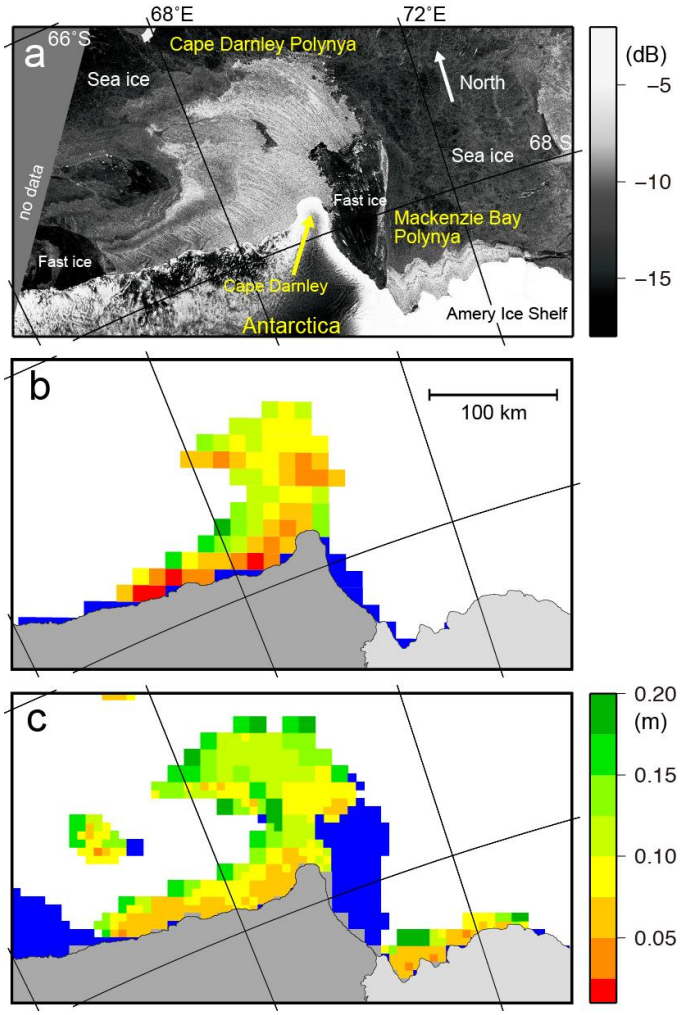

Fig. 1. (a) Radar backscatter image from Envisat ASAR of the region including the Cape Darnley Polynya and Mackenzie Bay Polynya acquired on 7 August 2008. Spatial resolution is about 150 m. (b) Thin ice thickness and fast ice on the same day, derived from SSM/I data, which are mapped onto a polar stereographic grid at a spatial resolution of about 12.5 km. (c) Thin ice thickness and fast ice derived from AMSR-E data, which are mapped onto a polar stereographic grid at a spatial resolution of about 6.25 km. In Figs. 1b and 1c (and also in Figs. 3b, 3d, 3f, 4, and 7), blue pixels indicate fast ice, the Antarctic continent and islands are shaded dark gray, and ice shelves and glacial tongues are light gray.

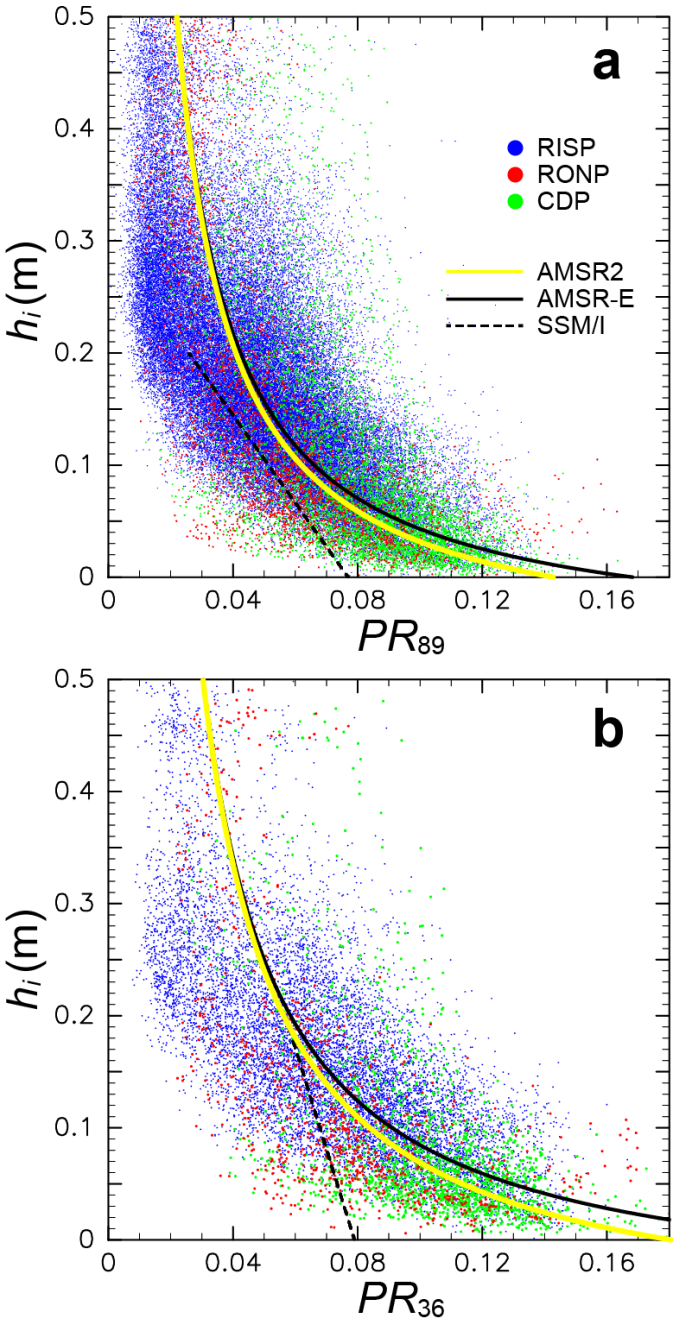

Fig. 2. (a) Scatterplot of PR_{89} from AMSR2 versus h_i from MODIS. (b) As in (a), but for use of PR_{36}. Blue, red, and green dots indicate data from areas of the Ross Ice Shelf Polynya (RISP), Ronne Ice Shelf Polynya (RONP), and Cape Darnley Polynya (CDP), respectively. Yellow lines are exponential curves (Eqs. 3 and 4) fitted to the data. Black solid and dashed lines indicate the relationship for AMSR-E [19] and SSM/I [17] data, respectively.

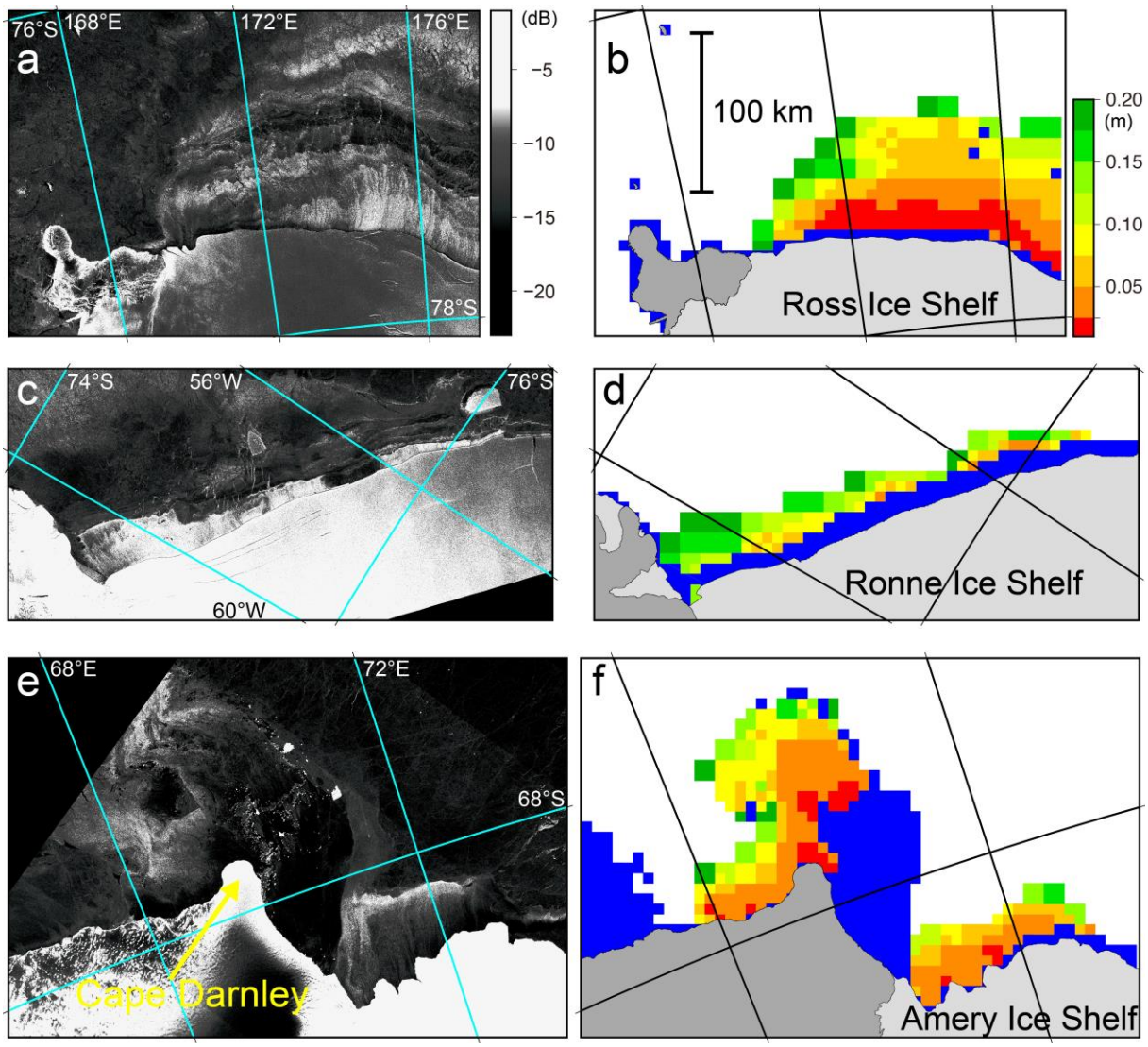

Fig. 3. Sea-ice backscatter and thin ice thickness around (a), (b) the Ross Ice Shelf Polynya on 12 April 2015, (c), (d) the Ronne Ice Shelf Polynya on 9 June 2015, and (e), (f) the Cape Darnley Polynya and Mackenzie Bay Polynya on 22 September 2015. (a), (c), and (e) Radar backscatter images acquired by Sentinel-1 C-SAR. The backscatter was obtained by taking into account the calibrations. Coastal polynyas appear as areas with white high-backscatter (>–15 dB) streaks; fast ice appears as a low-backscatter (< –20 dB) area east of the CDP in (e). (b), (d), and (f) Thin ice thickness and fast ice (blue) determined from AMSR2 data. The spatial scale is the same in all panels.

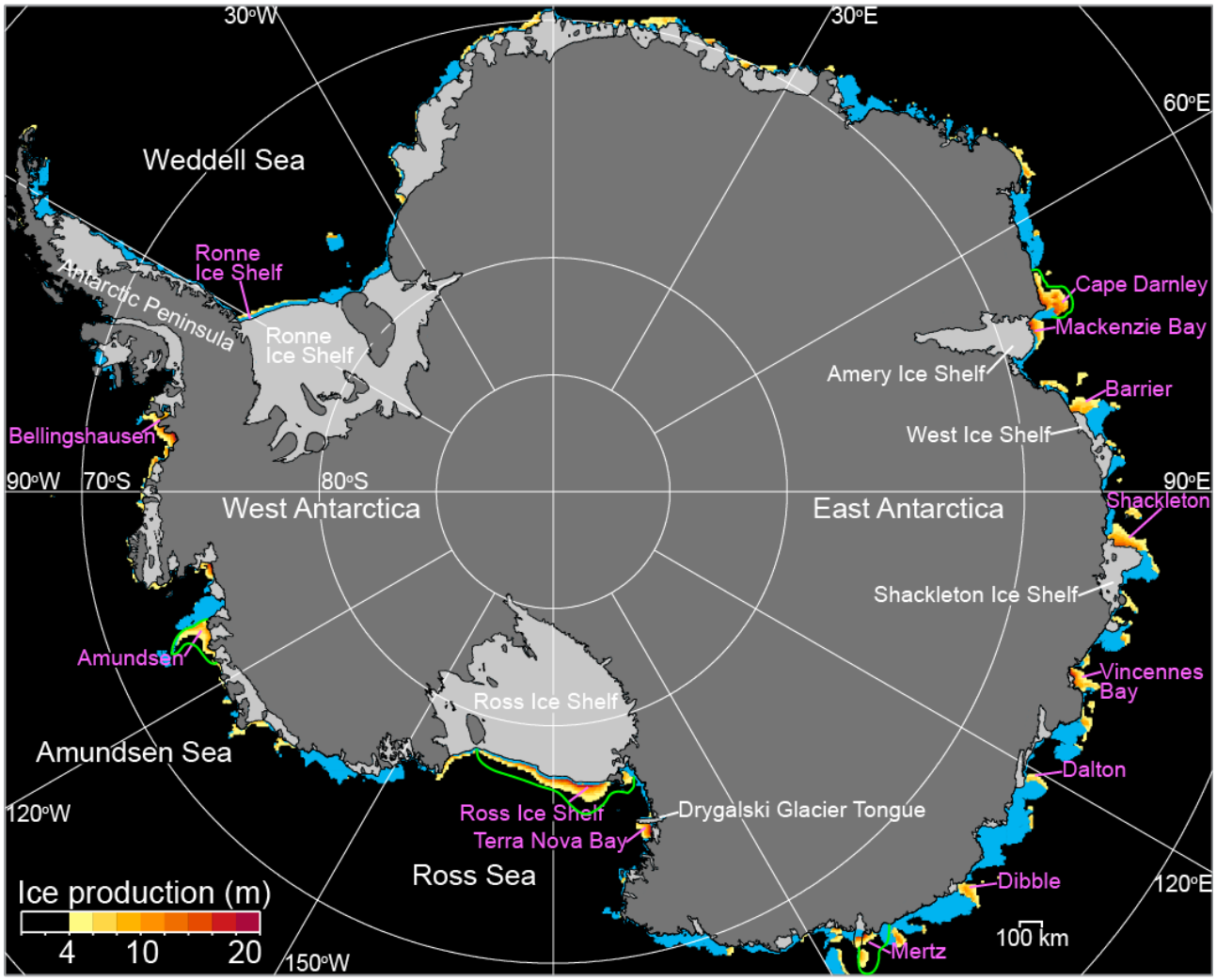

Fig. 4.

Map of annual ice production (cumulative ice production during March–October) averaged over 2013–2015. Fast ice areas are colored blue. Here the fast ice area is defined as a pixel whose occurrence frequency during the entire period is ≥60%. Analysis areas for ice production around the Cape Darnley, Mertz, Ross Ice Shelf, and Amundsen polynyas are enclosed by green lines. These areas were defined following previous studies [5] and [19].

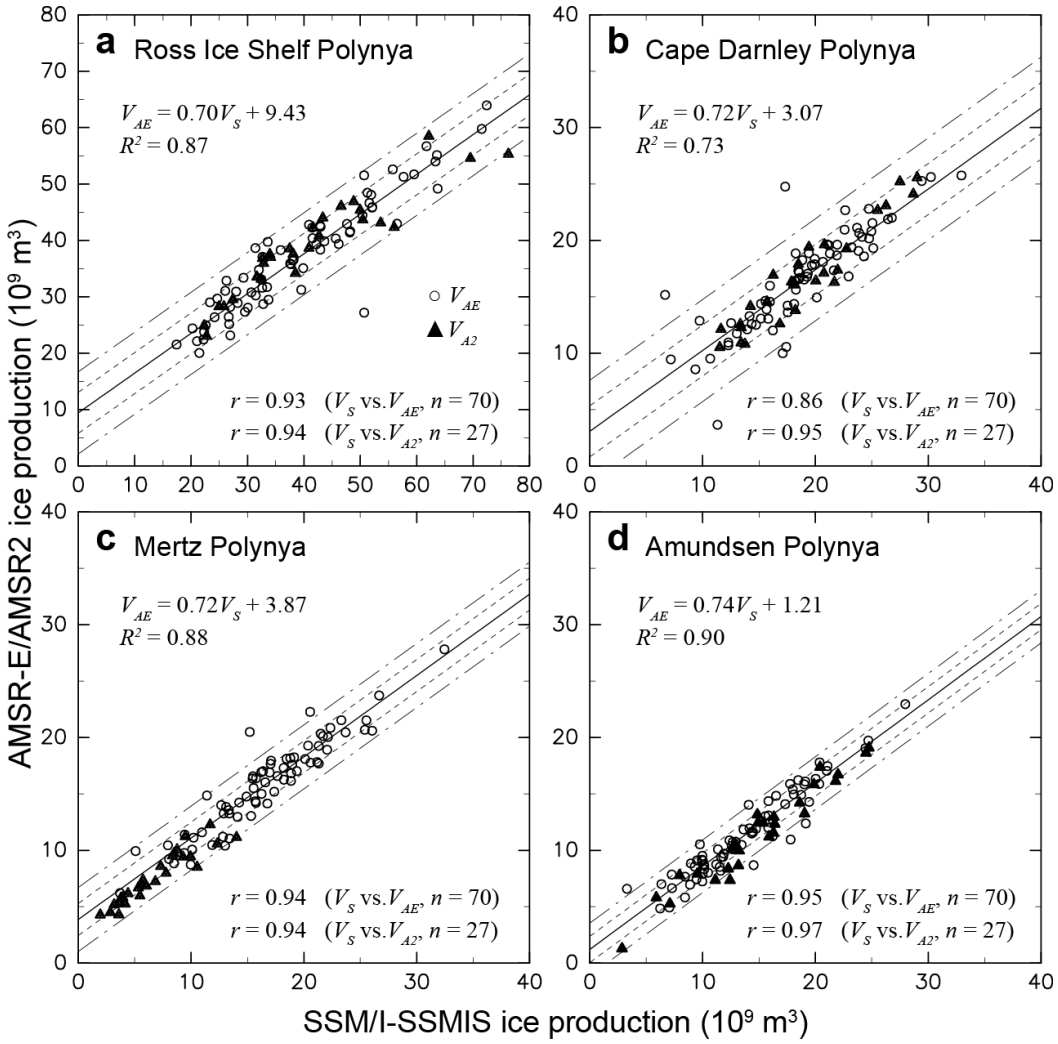

Fig. 5. Scatterplots of monthly ice production (10^9 m^3) of SSMI-SSMIS (V_s) versus AMSR-E (V_{AE}; circles) and AMSR2 (V_{A2}; triangles) in the Ross Ice Shelf Polynya, Cape Darnley Polynya, Mertz Polynya, and Amundsen Polynya areas shown in Fig. 4. We used monthly ice production during 70 months (March 2003 to August 2011) for the comparison between AMSR-E and SSM/I-SSMIS, and ice production during 27 months (August 2012 to October 2015) for the comparison between AMSR2 and SSM/I-SSMIS. The solid lines are regression lines obtained from the V_s—V_{AE} relationship by least-squares fitting. Dashed and dash-dotted lines indicate one- and two-standard deviations, respectively, from the regression line.

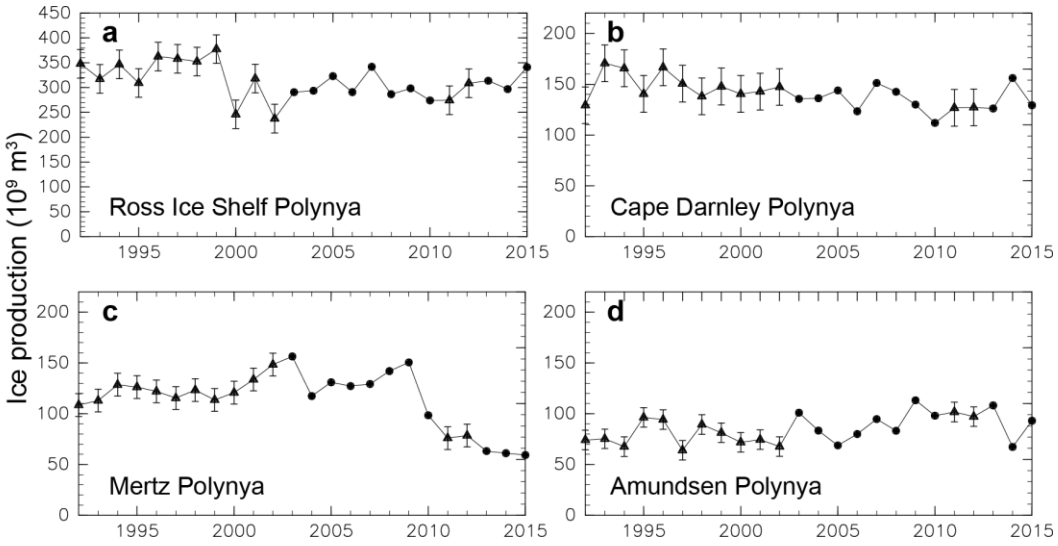

Fig. 6. Time series of annual ice production (cumulative ice production during March–October) in the Ross Ice Shelf Polynya, Cape Darnley Polynya, Mertz Polynya, and Amundsen Polynya areas. The analysis areas are shown in Fig. 4. Dots indicate ice production from AMSR-E (2003–2010) and AMSR2 (2013–2015) data, and triangles with error bars indicate ice production from SSM/I-SSMIS data. SSM/I-SSMIS ice production has been adjusted by using the regression lines in Fig. 5. The error bars indicate one standard deviation from the respective regression line (Fig. 5).

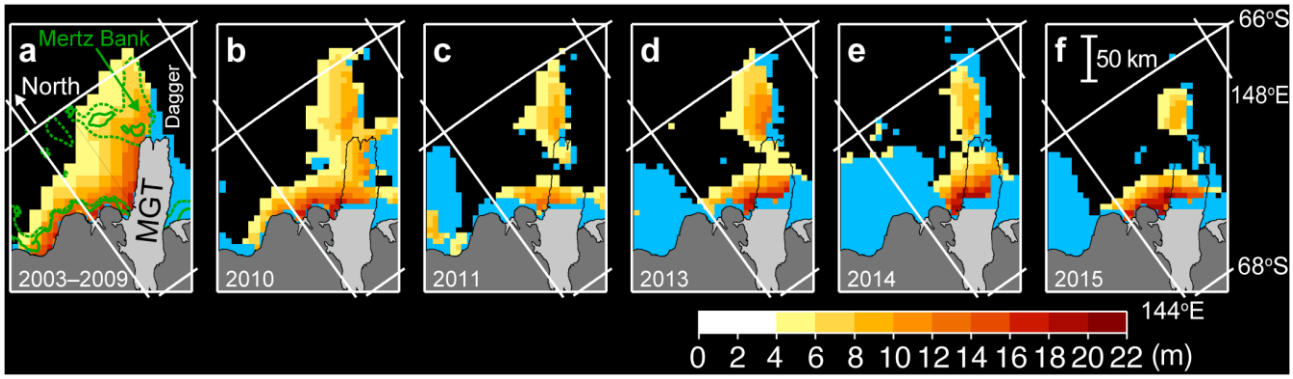

Fig. 7. Close-up maps of ice production in the Mertz Polynya area. (a) Annual ice production (cumulative ice production during March–October) from AMSR-E averaged over 2003–2009. The 200- and 300-m bathymetric contours are indicated by solid and dotted green lines, respectively. The bathymetry was obtained from the General Bathymetric Chart of the Oceans (GEBCO) One Minute Grid. (b) as in (a) but for 2010 when the Mertz Glacier Tongue (MGT) calving had occurred. (c) Cumulative ice production during March–August 2011 from AMSR-E. (d–f) Annual ice production from AMSR2 in 2013, 2014, and 2015, respectively. Fast ice areas are colored blue. To show fast ice dagger clearly, the fast ice area was defined as a pixel with an occurrence frequency during the period of ≥30%, which is different from Fig. 4 (≥60%).